Applied Catalysis B: Environmental 190 (2016) 36–43

Contents lists available at ScienceDirect

Applied Catalysis B: Environmental

journal homepage: www.elsevier.com/locate/apcatb

Dual synergetic effects in MoS_2/pyridine-modified g-C_3N_4 composite for highly active and stable photocatalytic hydrogen evolution under visible light

Mengli Li[a], Lingxia Zhang[a,*], Xiangqian Fan[a], Meiying Wu[a], Yanyan Du[a], Min Wang[a,b], Qinglu Kong[a], Linlin Zhang[a], Jianlin Shi[a,*]

[a] State Key Laboratory of High Performance Ceramics and Superfine Microstructure, Shanghai Institute of Ceramics, Chinese Academy of Sciences, Shanghai 200050, PR China
[b] School of Materials and Engineering, Shanghai University, Shanghai 200444, PR China

ARTICLE INFO

Article history:
Received 30 September 2015
Received in revised form 15 January 2016
Accepted 25 February 2016
Available online 27 February 2016

Keywords:
Hydrogen production
Dual synergetic effects
Photocatalysis
MoS_2
Graphite carbon nitride

ABSTRACT

Composite photocatalysts with nanoflower-structured MoS_2 grown on pyridine-modified graphitic carbon nitride (g-C_3N_4) have been synthesized through a facile *in situ* solvothermal approach. These composites demonstrate greatly enhanced response to visible light, and consequently remarkably enhanced hydrogen evolution performance by photocatalytic water splitting. The addition of 2,5-dibromopyridine during the formation process of g-C_3N_4 can not only enhance the photocatalytic activity but also the durability of the photocatalysts. The MoS_2 content and the ratio between 2,5-dibromopyridine and g-C_3N_4 in these composites can be well tuned to obtain the optimized photocatalytic activity with a peak H_2 production rate of 25 μmol h^{-1} on 50 mg photocatalyst without adding any noble metal under visible light irradiation at 283 K. A dual synergetic mechanism in MoS_2/pyridine-modified g-C_3N_4 composite, which is featured with significantly promoted separation of photo-generated carriers and stability of S^{2-} and/or S_2^{2-} in the composites under visible light irradiation, has been proposed to account for the distinguished hydrogen evolution activity and stability of these composite photocatalysts.

1. Introduction

Hydrogen is the cleanest energy fuel and will play an important role in the future energy system [1]. Photocatalytic water splitting to achieve sustainable hydrogen production has attracted growing attention and it is one of the most important pathways to produce hydrogen [2]. Since the report of hydrogen evolution from water in a photoelectrochemical cell by Fujishima and Honda in 1972, considerable studies have been focused on photocatalysts with high efficiency and stability, especially those consist of earth-abundant elements [3]. Among various semiconductors, the graphitic carbon nitride (g-C_3N_4) with two-dimensional (2D) structures is indeed an attractive type of visible-light photocatalyst because of its suitable electronic structure (Eg = 2.7 eV, conduction band at −0.8 V and valence band at 1.9 V *vs.* RHE), large surface area and excellent chemical stability [4–6]. However, its photocatalytic efficiency is still moderate because of the fast recombination of photo-generated charge carriers and the mismatch between its band gap and solar radiation spectrum.

The photocatalytic performance of g-C_3N_4 has been greatly enhanced by simply copolymerizing barbituric acid with the carbon nitride precursor through a Schiff base reaction [7,8]. The construction of g-C_3N_4-based intramolecular donor-acceptor conjugated copolymers have been reported by our group, which showed elevated activity of g-C_3N_4 for hydrogen evolution [9,10]. Another widely reported approach to enhance its activity is to couple g-C_3N_4 with other semiconductors. It is reported that coupling g-C_3N_4 with other layered semiconductors to construct a heterojunction or heterostructure is an effective strategy for improving its photocatalytic activity [11]. The construction of layered junction is considered to be able to increase the contact area for efficient charge transfer across the interface and shorten the charge transport time and distance, thereby promote the separation of photo-

* Corresponding authors.
E-mail addresses: zhlingxia@mail.sic.ac.cn (L. Zhang), jlshi@mail.sic.ac.cn (J. Shi).

http://dx.doi.org/10.1016/j.apcatb.2016.02.060
0926-3373/

generated electron-hole pairs and lead to enhancement of overall photo conversion efficiency [12]. Therefore, it is highly desirable to develop a new modification method and/or coupling g-C_3N_4 with other layered semiconductors to form a heterostructured photocatalyst with improved photo conversion efficiency [12–15]. Recently, two-dimensional (2D) molybdenum disulfide (MoS_2) has received considerable attention because of its outstanding properties and potential applications in catalysis, energy storage, biology, electronics etc. [16]. Among various catalysts for hydrogen-evolution, MoS_2 with exposed edges has received a lot of attention due to its low cost and excellent electrical conductivity [17,18]. MoS_2 has a similar structure with g-C_3N_4, and is composed of layered crystal structure consisting of S-Mo-S "sandwiches" held together by van der Waals force. Recently, MoS_2 and Pt co-loaded g-C_3N_4 for highly efficient H_2 production has been obtained *via* an impregnation method [19]. Hydrothermal synthesis has also been reported to prepare MoS_2 and Pt co-decorated g-C_3N_4, which exhibited high photocatlytic activity and good stability for the decoloration and degradation of methyl orange under simulated solar light [20]. Thin-layered MoS_2 combined with g-C_3N_4 has been obtained by a thermal deposition process, which showed high photocatalytic activity for H_2 production [21]. Among these methods, for impregnation strategy, MoS_2 was firstly prepared under high temperature and high pressure conditions, and subsequent heat treatment was necessary to combine MoS_2 and g-C_3N_4. In the hydrothermal synthesis and thermal deposition process, toxic $NH_2OH{\cdot}HCl$ and H_2S had to be used, respectively, both of which are harmful to the environment. More importantly, the stability of the reported MoS_2/g-C_3N_4 heterojunctions for H_2 evolution was still far from satisfactory. MoS_2/g-C_3N_4 catalyst lost about 25% of its initial activity after 16 h cycle durability tests [21]. Therefore, it is still an urgent and big challenge to develop novel and facile strategies to fabricate high active and stable MoS_2/g-C_3N_4 photocatalyst.

Herein, a novel kind of MoS_2/g-C_3N_4 heterostructured photocatalysts has been prepared *via* an *in situ* solvothermal method. Firstly, 2,5-dibromopyridine was used to modify g-C_3N_4, and an intramolecular donor-acceptor (D-A) conjugated polymer was obtained. Then MoS_2 was *in situ* grown on the D-A copolymer using $(NH_4)_2MoS_4$ as a precursor. The as-synthesized heterostructure showed significant visible light sensitivity, highly efficient separation and transfer property of charge carriers, which was greatly helpful for its high activity in hydrogen evolution. More interestingly, for the first time, the high stability of MoS_2/g-C_3N_4 heterostructure on H_2 evolution under visible light irradiation has been reported.

2. Experimental

2.1. Synthesis procedure

All reagents, including $(NH_2)_2CO$ (AR, Sinapharm Chemical Reagent Corp, P.R. China), $(NH_4)_2MoS_4$ (AR, Shanghai J&K, China) and 2,5-dibromopyridine (AR, Sigma-Aldrich) are used directly without any further purification.

The pyridine modified graphitic carbon nitride (g-C_3N_4), denoted as CN-Py, was synthesized by a facile calcination method. In detail, 20 g urea and 1 g 2,5-dibromopyridine were mixed thoroughly and placed in a crucible with a cover under ambient pressure in air. The crucible was put in a Muffle Furnace and heated to 550 °C for 2 h with a ramp rate of 4 °C min^{-1}. Finally, the crucible was cooled to room temperature naturally. The possible reaction path of CN-Py formation is listed in Scheme S1. The g-C_3N_4 was obtained by the same method without addition of 2,5-dibromopyridine. The resulting products were collected and ground into fine powder for further use.

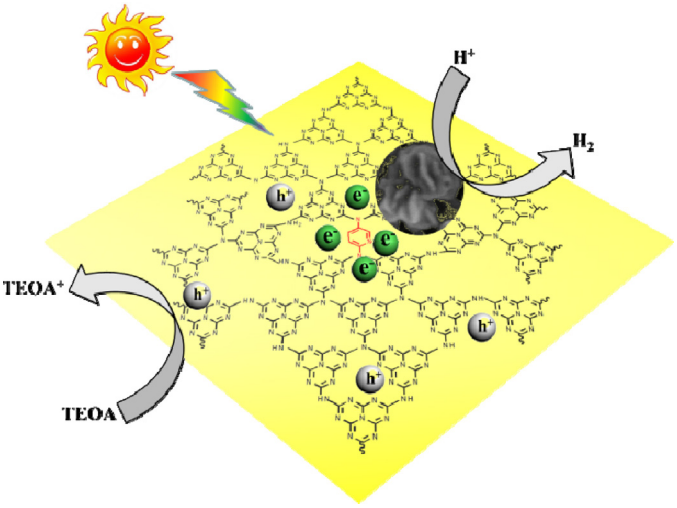

Scheme 1. Schematic illustrations of the dual synergetic catalytic mechanism in the MoS_2/CN-Py heterostructures. (1) mutual activation between the CN-Py support and MoS_2: Electron and hole pairs are generated in MoS_2/CN-Py under visible light irradiation, and the electrons generated on the conduction band of CN-Py will tranfer to that of MoS_2, which benefits the efficient separation of photogenerated electrons and holes in CN-Py. The activated H_2O can be reduced to H_2 by electrons on MoS_2, while TEOA can beoxidzed to $TEOA^+$ by holes on CN-Py. (2) the photo-corrosion prevention of MoS_2 by the CN-Py support for sustained photocatalytic activity: The photo-induced electrons located at the elevated conduction band level of CN-Py have stronger photoreduction ability, which can effectively suppress the oxidation of S^{2-} and/or S_2^{2-} in MoS_2 and thus ensure the stability of the catalysts.

The pure MoS_2 nanoflowers assembled by densely packed petals were synthesized by a modified solvothermal method [22]. The MoS_2/CN-Py and MoS_2/g-C_3N_4 heterostructured photocatalysts were obtained by a solvothermal method using CN-Py or g-C_3N_4 and the precursors of MoS_2. In a typical procedure, certain amounts of $(NH_4)_2MoS_4$ and 0.3 g CN-Py or g-C_3N_4 were mixed in 30 mL N, *N*-dimethylformamide (DMF). The mixture was consecutively sonicated at room temperature for approximately 20 min until black homogeneous slurry was achieved. After that, the obtained mixed solution was then placed in an 80 mL Teflon-lined autocalve maintaining at 200 °C for 10 h in an oven. The resulting samples were collected by centrifugation, washed several times with deionized water and lyophilized overnight and denoted as *x*% MoS_2/CN-Py or *x*% MoS_2/g-C_3N_4, respectively, where *x* represents the weight content of MoS_2.

2.2. Characterization

The crystallographic phase of the prepared photocatalysts was determined by a Rigaku D/Max 2200 PC X-ray diffractometer (XRD) with a scanning rate of 4° min^{-1}. The X-ray tube using Cu *Kα* radiation was operated at 40 kV and 40 mA in the 2θ range of 10–80°. The specific surface area of the samples was characterized using Micromeritics Tristar 2000 instrument at 77 K and calculated by the Brunauer Emmett Teller (BET) method. Transmission electron microscopy (TEM), selected area electron diffraction (SAED) patterns and energy dispersive spectrometer (EDS) were obtained by JEM-2100F field emission transmission electron microscope (FE-TEM) operated at 200 kV. Field emission scanning electron micrograph (FE-SEM) was acquired on a Hitachi S-4800. The UV–vis absorption spectra was recorded between 200 and 800 nm on a UV-3101 PC Shimadzu spectroscope using $BaSO_4$ as a reference. The photoluminescence (PL) spectra of the as-prepared samples were measured using a Hitachi F-4500 fluorescene spectrophotometer with an excitation wavelength of 370 nm at room temperature. X-ray photoelectron spectroscopy (XPS) data was carried out on a

Thermo Scientific ESCALAB 250 spectrometer with an Al *Kα* radiation line source and the binding energies for the high resolution spectra were calibrated by setting C 1 s to 285 eV. High resolution Fourier transform infrared (FTIR) spectra were conducted on a Nicolet iZ10 Fourier transform infrared spectrometer at a resolution of 4 cm^{-1}.

2.3. Electrochemical measurements

The photocurrent measurements were carried out on a CHI 660A electrochemical workstation (Chenhua Instrument, Inc.) with a conventional three-electrode cell. Fluorine-doped Tin Oxide (FTO) deposited with photocatalysts served as a working electrode, while the reference and the counterelectrodes were a platinum wire and Ag/AgCl respectively, with 0.1 M Na_2SO_4 aqueous solution as electrolyte. The working electrodes were prepared by electrophoretic deposition method. The visible light was generated by a 300 W Xe lamp with an UV cut-off filter (λ > 420 nm) and was chopped manually. The EIS spectra of g-C_3N_4, CN-Py, and 3% MoS_2/CN-Py electrodes were obtained in 50 mL 0.2 M Na_2SO_4 aqueous solution at −0.4 V *vs.* Ag/AgCl electrode in dark.

A Pt wire and an Ag/AgCl electrode were also used as the counter and reference electrodes, during the Mott-Schottky test. The working electrode was prepared as follows. The electrode's area is about 1.5 cm^2. 80 mg of sample, 10 mg of carbon black and 10 mg of polyvinylidene fluoride (PVDF) binder were mixed in ethanol. 10 mg of the mixture was pasted onto a nickel foam current collector. Mott-Schottky plots were generated with a frequency of 962 Hz.

2.4. Photocatalytic activity evaluation

The visible light photocatalytic hydrogen-production experiments were performed in a Pyrex top-irradiation reaction vessel connected to a closed glass gas-circulation system (Lab Soalar-III AG, Perfectlight Limited, Beijing) and evacuation system. A 300 W Xenon lamp (PLS-SEX 300C, Perfectlight Limited, Beijing) with a UV cutoff filter (λ > 420 nm), which was positioned 10 cm away from the reactor, served as the irradiation light source to trigger the photocatalytic reaction. In a typical photocatalytic experiment, 50 mg of catalyst was suspended in 100 mL aqueous solution containing triethanolamine (10 vol%) as the sacrificial electron donor. The suspension was thoroughly degassed before irradiation. The temperature of the reactant solution was maintained at 283 K by a flow of cooling water during the reaction. The evolved hydrogen was intermittently sampled every 1 h and analyzed by a gas chromatograph (GC 7900, Techcomp) equipped with a 5A molecular-sieve column and a thermal-conductivity detector. For stability test, the system was evacuated every 5 h and repeated for 5 times.

3. Results and discussion

3.1. Characterization of the as-prepared samples

XRD patterns of the synthesized heterostructured composites, as well as those of pure CN-Py, are shown in Fig. 1. All samples exhibit two distinct peaks. The XRD peaks at around 27.4° and 13.1° can be indexed as the (0 0 2) and (1 0 0) reflections, corresponding to the interlayer stacking and in-plane structure packing motif of carbon nitride, respectively [23–25]. No obvious peaks related to MoS_2 can be found in the hetereostructured samples, which reveals that loading with MoS_2 does not change the bulk structure and chemical skeleton of CN-Py. For pure MoS_2, the broad diffraction peaks at around 57° and 35° (seen in Fig. S1) indicate nanosized MoS_2 crystals are dominated with hexagonal structure [powder diffraction file (PDF) No. 771716] and they can be indexed as the (1 1 0) and (1 0 0) reflections, respectively. In order to verify whether the aromatic groups of 2,5-dibromopyridine have been successfully grafted in the CN-Py structure, g-C_3N_4 and CN-Py were selected to conduct high resolution FT-IR as shown in Fig. 2. The sample CN-Py exhibits an extra weak IR band at around 1507 cm^{-1}, which is attributed to aromatic C=C signal. This aromatic C=C signal can still be detected and its relative intensity changes little after long-time ultrasound treatment and washing for several times as shown in Fig. S2, further confirming the successful pyridine grafting.

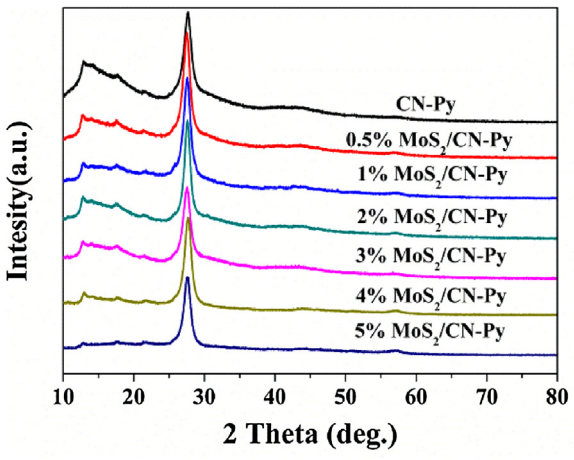

Fig. 1. XRD patterns of CN-Py, and MoS_2/CN-Py samples.

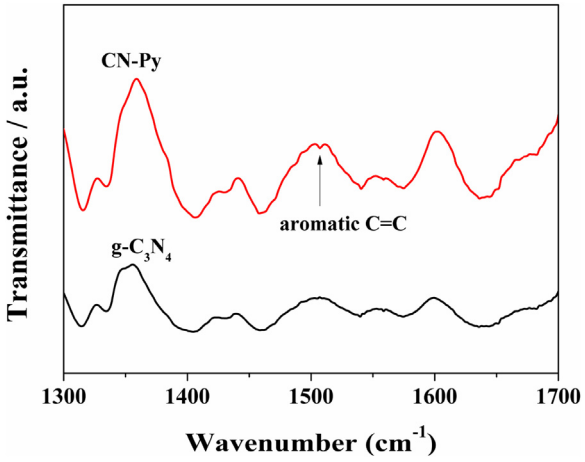

Fig. 2. High-resolution FT-IR spectra of g-C_3N_4 and CN-Py.

In order to analyze the textural properties of these as-prepared samples, the N_2 adsorption-desorption isotherms at 77 K were measured. In Fig. 3, typical H4 hysteresis loops can be observed at P/P_0 = 0.9– 1.0, which is the characteristic of mesoporous structure. The calculated BET specific surface area of CN-Py is about 74.2 $m^2\ g^{-1}$. The BET specific surface area of the composites gradually decreases with the increasing content of MoS_2, and the specific surface areas of 0.5% MoS_2/CN-Py and 3% MoS_2/CN-Py samples are 46.5 and 16.4 $m^2\ g^{-1}$, respectively. Their average pore diameters are about 10–30 nm as shown in the inset table.

Field-emission scanning electron microscopy (FE-SEM) and Transmission electron microscopy (TEM) were employed to directly analyze the morphology and microstructure of the samples. Fig. 4a shows uniform flower-like morphology of pure MoS_2 formed by the accumulation of MoS_2 nanosheets. The curly and folded thin nanosheets of ~2 nm in thickness branch out from one central zone. As shown in Fig. 4b, a typical aggregated morphology with a large size and lamellar structure of CN-Py can be found in

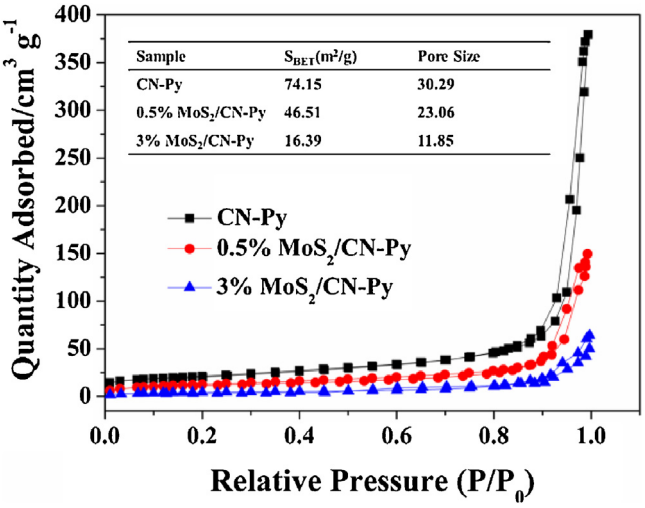

Fig. 3. N_2 adsorption-desorption isotherms of CN-Py, 0.5% MoS_2/CN-Py and 3% MoS_2/CN-Py. Inset table shows the calculated specific surface area and pore size of the samples.

the 3% MoS_2/CN-Py sample. The element mappings (Fig. S3) of the composite imply the interspersion between MoS_2 and CN-Py. The selected area electron diffraction (SAED) pattern recorded on the 3% MoS_2/CN-Py sample shows two sets of diffraction signals: the two separated diffraction rings can be well indexed to the (1 1 0) and (1 0 0) planes of the polycrystalline hexagonal MoS_2 [26]. The magnified high-resolution TEM (HRTEM) image in Fig. 4d displays a fringe with a lattice d-spacing of approximate 0.62 nm, corresponding to the (0 0 2) plane of hexagonal MoS_2.

As it is known to all, the semiconductor photocatalytic process consists of photo excitation, the separation and transfer of photo-induced charge carriers or the recombination of photo-induced charge carriers, the generation of active species, and subsequent chemical reactions [27,28]. Among these processes, the principal photo excitation indispensably depends on the semiconductor's bandgap. Therefore, it is quite important to understand the effect of MoS_2 on the optical absorption property and photoluminescene (PL) of the hetereostructured composites. As shown in Fig. 5a, the optical property of CN-Py and the MoS_2/CN-Py composites were characterized using UV–vis diffuse reflectance spectroscopy (DRS). All the samples absorb UV to visible light as expected, which signifies their visible-light-induced photocatalytic hydrogen generation activity. The absorption onset of the CN-Py is at 455 nm, corresponding to the band gap of 2.73 eV. The addition of MoS_2 remarkably alters the optical properties of CN-Py. Compared with CN-Py, the MoS_2/CN-Py composites show much enhanced absorption in visible light range. Their absorption intensity increases with the increasing MoS_2 content. The enhanced light adsorption ability of the composite photocatalyst will greatly improve the light utilization and consequently enhance its photocatalytic performance.

Photoluminescence (PL) and EIS analyses were performed to study the interfacial charge transfer and the separation efficiency of photo generated carriers in photocatalysts. PL spectra of CN-Py and all the MoS_2/CN-Py composites are shown in Fig. 5b. Under 370 nm excitation at room temperature, all the luminescence spectra of these photocatalysts show a broad peak centered at around 455 nm with a tail extending to 600 nm. The emission could be attributed to the band–band recombination of the photogenerated charge carriers with its emission photon energy being equal to its bandgap energy. Obvious PL quenching can be observed for samples by the addition of MoS_2. However, the PL intensity decreases with the increasing content of MoS_2. Compared with CN-Py,

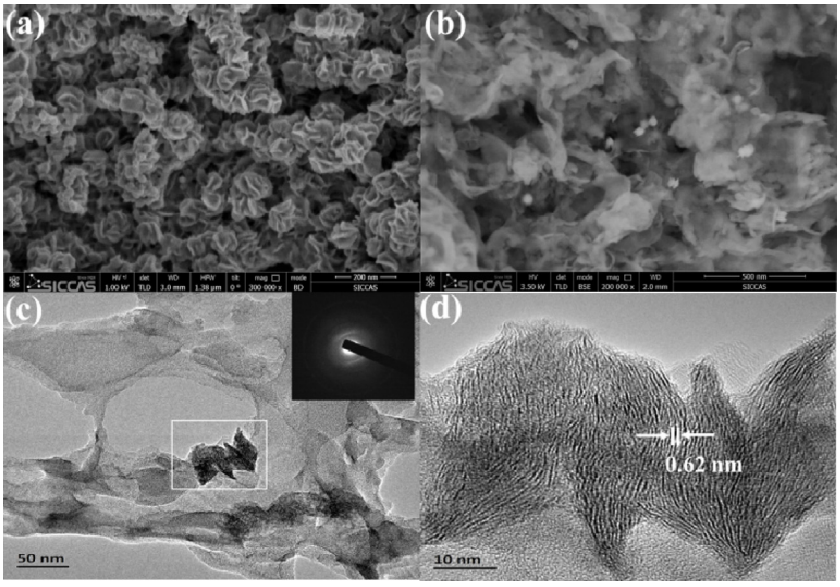

Fig. 4. SEM images of (a) MoS_2 and (b) 3% MoS_2/CN-Py; (c) TEM image and inserted SAED pattern and (d) the magnified HR-TEM image of the selected area from (c).

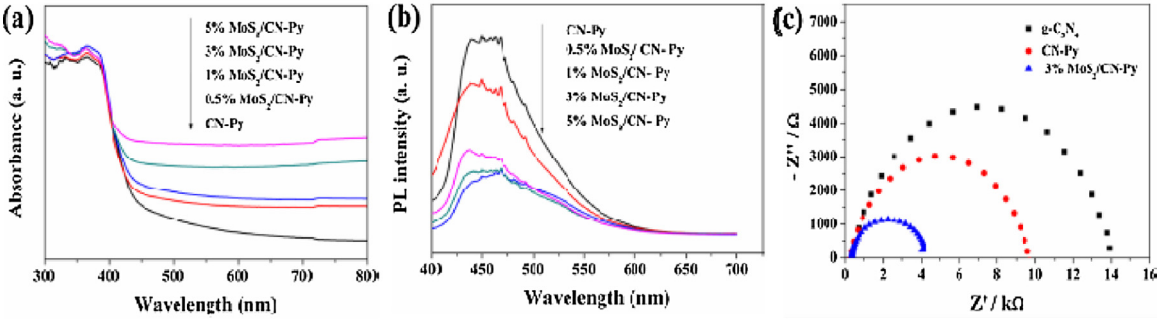

Fig. 5. (a) UV–vis diffuse reflectance spectra of the as-prepared samples, (b) Photoluminescence spectra at an excitation wavelength of 370 nm, and (c) Nyquist plots of electrochemical impedance spectroscopy of g-C_3N_4, CN-Py, and 3% MoS_2/CN-Py electrodes at −0.4 V *vs.* Ag/AgCl in 50 mL 0.2 M Na_2SO_4 aqueous solution in dark.

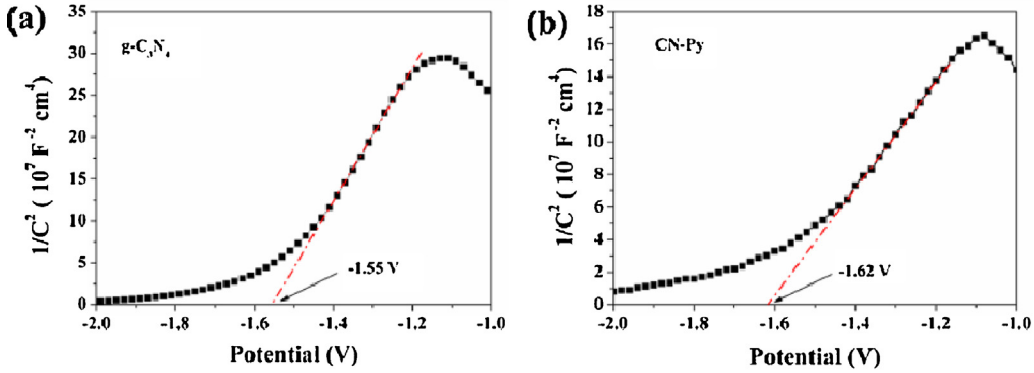

Fig. 6. Mott-Schottky plots collected ong-C_3N_4 (a) and CN-Py (b) at a frequency of 962 Hz in dark.

MoS_2/CN- Py composites showed much lowered PL intensity. The presence of MoS_2 should promote charge transfer between MoS_2 and CN-Py components. The charge transfer in dark was studied by EIS to verity this assumption. As shown in Fig. 5c, for each sample, only one semicircle emerges in the spectrum, indicating that only surface charge-transfer is involved in the photocatalytic reaction system [29]. It can be found that the semicircular diameter of g-C_3N_4 is the largest, while that of 3% MoS_2/CN-Py is the smallest, reflecting that the addition of 2,5-dibromopyridine and MoS_2 can accelerate the electron transfer [30,31]. This is an indication of a lower recombination rate of visible-light excited electrons and holes in the composite, and/or more efficient electron relocalization on the surface terminal sites, which is believed to be beneficial for elevating photocatalytic reactivity under visible-light irradiation [32,33].

In order to further study the influence of 2,5-dibromopyridine addition, Mott-Schottky tests were carried out to confirm the electronic potentials of g-C_3N_4 and CN-Py, as shown in Fig. 6. The measured potentials can be converted to the reversible hydrogen electrode (RHE) scale via the Nernst equation:

$$E_{RHE} = E_{Ag/AgCl} + 00.05916\ pH + E^0_{Ag/AgCl}$$

where E_{RHE} is the converted potential *vs.* RHE, $E_{Ag/AgCl}$ is the experimental potential measured against the Ag/AgCl reference electrode, while $E^{\circ}_{Ag/AgCl}$ is the standard potential of Ag/AgCl at 298 k (0.1976 V). The calculated conduction band edges of g-C_3N_4 and CN-Py are −1.55 eV and −1.62 eV, respectively, which implies that the sample CN-Py has stronger reducibility than g-C_3N_4 and the photo-generated electrons in CN-Py are less likely to recombine with photo-generated holes.

The excitation and transfer of photogenerated charge carriers in the pure g-C_3N_4, CN-Py and 3% MoS_2/CN-Py were qualitatively investigated by photoelectrochemical measurements. Fig. 7 shows the photocurrent responses during three on-off cycles. It is clear that the photocurrent intensity of the heterostructured composite 3% MoS_2/CN-Py (3.5 μA cm^{-2}) is more than three times higher than that of CN-Py (0.85 μA cm^{-2}) under visible light irradiation, indicating that the composite may achieve more effective charge separation and higher photocatalytic activity than single component CN-Py or pure g-C_3N_4. Besides, it is interesting that the photocurrent intensity of CN-Py is about two times that of pure g-C_3N_4, which means that the addition of 2, 5-dibromopyridine is in favor of the efficient separation of photo-generated carriers under visible light irradiation [9].

To further investigate the interaction between MoS_2 and CN-Py, XPS spectra were recorded and shown in Fig. 8. Both the valence states and the composition of the MoS_2/CN-Py were characterized. Fig. 8a confirms the presence of O, N, C, Mo and S. The C 1s spectrum shown in Fig. 8b can be deconvoluted into two peaks at 285 and 288.5 eV, which can be ascribed to the C—C coordination or sp^2 C=C bonds of the surface adventitious carbon and sp^2 bonded carbon (N—C=N) in triazine rings, respectively [34]. The high-resolution XPS of Mo 3d regioncan be deconvoluted into five peaks as shown in Fig. 8c. One peak at 226.3 eV is actually assigned to S 2s. The other two main intense peaks at 228.7 eV and 232.1 eV are characteristic signals of Mo $3d_{5/2}$ and Mo $3d_{3/2}$, respectively. Furthermore, we observed a binding energy peak at 235.4 eV assigned to Mo^{6+} in MoO_3 or MoO_4^{2-}, presumably owing to the formation of small amounts of surface oxide species [35,36]. The shoulder peak at around the binding energy of 230.1 eV indicates that Mo^{6+} has been partially reduced to Mo^{5+} which is present in the sulfide as an intermediate phase [22]. In addition to Mo element, sulfur species were further determined from the high-resolution XPS spectrum of S 2p (Fig. 8d). The main doublet located at 161.8 and 163.5 eV corresponds to the S $2p_{3/2}$ and S $2p_{1/2}$ of MoS_2, respectively. Meanwhile, the binding energy at 164.8 eV suggests the existence of both bridging disulfides $S_2^{2-}$and S^{2-} ligands [37]. The peak at 168.7 eV

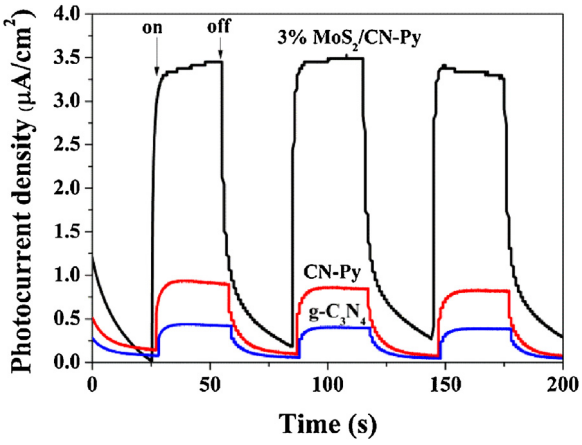

Fig. 7. Periodic on/off photo-responses of g-C_3N_4, CN-Py and 3% MoS_2/CN-Py electrodes. All the electrodes were evaluated in 0.1 M Na_2SO_4 aqueous solution under visible light irradiation using Ag/AgCl as reference electrode.

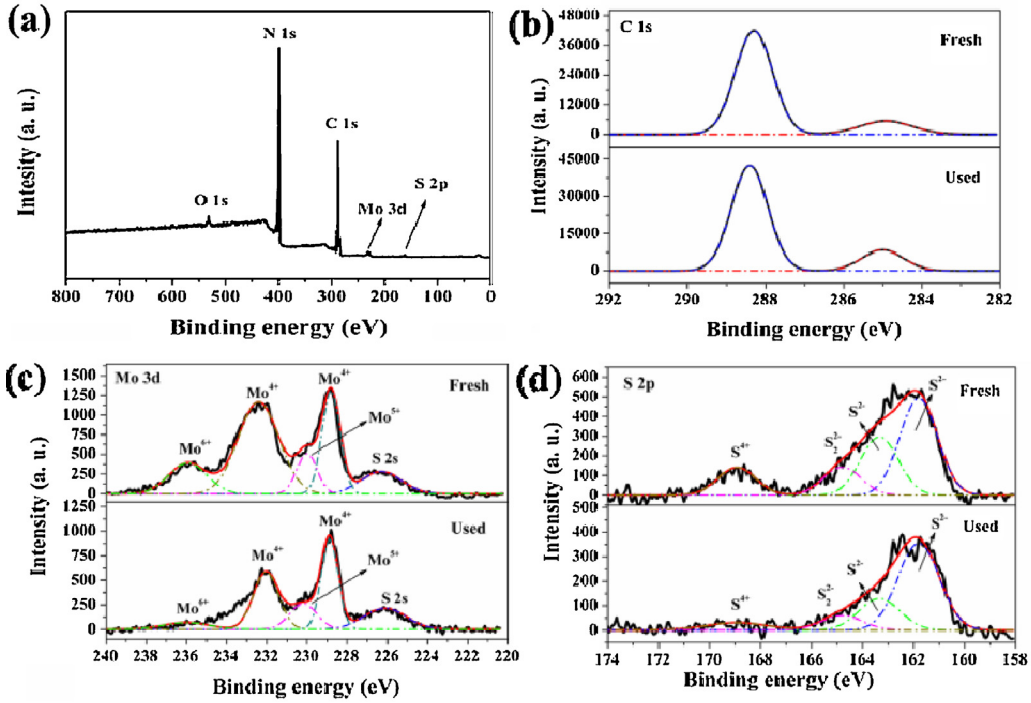

Fig. 8. X-ray photoelectron spectra of (a) 3% MoS_2/CN-Py, high-resolution spectra of (b) C 1s, (c) Mo 3d, (d) S 2p in fresh and used 3% MoS_2/CN-Py.

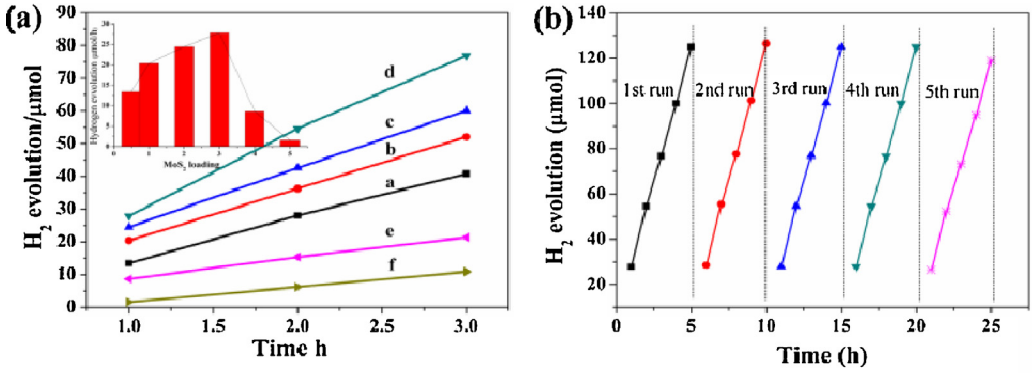

Fig. 9. Photocatalytic H_2 production under visible-light irradiation on (a) 0.5% MoS_2/CN-Py (a); 1% MoS_2/CN-Py (b); 2% MoS_2/CN-Py (c); 3% MoS_2/CN-Py (d); 4% MoS_2/CN-Py (e); 5% MoS_2/CN-Py f); The inset figure exhibits the amounts of H_2 produced in the first hour over x% MoS_2/CN-Py. (b) Cycle runs for the photocatalytic H_2 production on 3% MoS_2/CN-Py.

can be assigned to S^{4+} species in sulfate groups (SO_3^{2-}). Note that these groups could be located at edges of MoS_2 layers and would be still present even after being washed with a salt solution. In order to investigate the chemical stability of MoS_2/CN-Py photocatalyst, XPS analysis of the used sample in H_2 evolution experiment has also been conducted. It is notable that the changes observed in Mo 3d and S 2s core level spectra of fresh and used samples are quite different from those reported [21]. The data obtained after deconvolution (see the Supporting Information, Table S1) reveal that the atomic ratio of S^{4+} decreases significantly after a 25 h cycle experiment, which is believed to be responsible for the excellent stability of the composite MoS_2/CN-Py in the following H_2 evolution experiment. Finally, for pure MoS_2 nanoflowers, the analysis of the peak intensities of Mo 3d and S 2p yields an S/Mo atomic ratio of 2.11.

3.2. Photocatalytic activity of the samples

The photocatalytic activities of the photocatalysts were measured in a gas-closed circulation system operated under vacuum condition. The hydrogen generated in the system was continually taken from the reaction cell at given intervals (1 h) for subsequent quantitative analysis based on the external standard method and the calibration curve. The composites usually show significant synergetic effect during photoreduction reaction [38]. Because of the anisotropic conductivity of MoS_2 [39], thin-layered MoS_2 is capable of promoting charge transfer from layer to layer and shorten the electron transport distance, thus resulting in the elevated utilization efficiency of photo-generated electrons for hydrogen production. It can be seen that all composite catalysts show good hydrogen evolution activities and the production rates of H_2 were in the order of $\mu mol\ h^{-1}$ as shown in Fig. 9 . Significantly, the H_2 production rate reaches the highest of 25 $\mu mol\ h^{-1}$ at the 3 wt% loading amount of MoS_2 (Fig. 9a). Lower or higher amounts of MoS_2 loading results in decreased hydrogen evolution rates, which can be likely attributed to the insufficient MoS_2 loading and the shading effect on CN-Py by MoS_2, respectively [21].

A 25 h experiment with intermittent evacuation every 5 h on 3% MoS_2/CN-Py under visible light irradiation was performed to examine the stability of the composite catalyst as shown in Fig. 9b. The system produced 125 μmol H_2 in 5 h during the former four cycles without noticeable deactivation. Only a slight decrease of H_2 amount (119.1 μmol) has been found during the fifth cycle. Obviously, compared to the literature reports so far found, the present heterostructured composite shows substantially enhanced stability for photocatalyzed hydrogen evolution.

In order to study the influence of 2,5-dibromopyridine, the parallel experiments were carried out as shown in Fig. S4. The amounts of H_2 produced on MoS_2/CN-Py are about 2.5 times as many as that on MoS_2/g-C_3N_4. In another word, the pyridine-modified photocatalysts show much higher activity than the pristine ones, no matter how much MoS_2 was loaded. To study how the ratio between 2,5-dibromopyridine and urea influences the photocatalysts' activity, a series of 3% MoS_2/CN-Py-*y* samples were synthesized and tested (shown in Fig. S5), where *y* stands for the added 2,5-dibromopyridine amount by the gram during the preparation process of CN-Py.

To verify the universality of this modification strategy, 3% WS_2/g-C_3N_4 and 3% WS_2/CN-Py were synthesized by the same solvothermal method by using $(NH_4)_2WS_4$ instead of $(NH_4)_2MoS_4$ as precursor. No detectable H_2 was obtained over pure g-C_3N_4 or MoS_2 under identical conditions described above. Compared to 3% WS_2/g-C_3N_4, 3% WS_2/CN-Py shows enhanced hydrogen evolution activity and stability as shown in Fig. S6.

4. Dual synergetic catalytic effects for enhanced activity and stability

The photocatalytic process of H_2 production on this MoS_2/CN-Py heterostructure can be depicted in Scheme 1. It is known to all that the hydrogen evolution activity of a semiconductor is determined by its energy level of photo-induced electrons, band gap width, surface area and the separation efficiency of charge carriers, etc. In this heterostructured system, the two components, MoS_2 and CN-Py, are proposed to interact with each other which results in significant dual synergetic effects: MoS_2 and CN-Py can be mutually activated under visible light irradiation for enhanced photocatalytic activity in one hand; and the degradation of one component (MoS_2) due to decomposition under light illumination can be prevented by the other (CN-Py) for sustained catalytic reaction in the other hand, according to a recent review on synergetic catalytic effects [38].

Specifically, similar to the most elaborately designed combinations between two semiconductors, MoS_2 can accelerate the transfer process by forming surface heterostructure with CN-Py and establishing electron transport chains. The MoS_2/CN-Py composites have a typical type-I heterostructure [39], in which both the VB and CB edges of one semiconductor are localized within the energy gap of the other one. The electron-hole pairs in both MoS_2 and CN-Py can be split apart under visible light irradiation as mentioned above, i.e., light irradiation induces the generation and separation. Afterward, driven by the contact electric filed, part of the photogenerated electrons in CN-Py will transfer to the interface between MoS_2 and CN-Py and to MoS_2, resulting in enriched electrons at the interface and in MoS_2, while holes stay on CN-Py [40]. The electron-transfer from the CB of CN-Py to the interface and the CB of MoS_2 results in efficient charger carrier separation, thus enhances the photocatalytic activity of this composite system and prevents MoS_2 from photo-corrosion. Such a charge transfer and recombination prevention process can be regarded as the mutual activation between CN-Py and MoS_2 [41], as illustrated in Scheme 1. The unsaturated active S atoms on the exposed edges of MoS_2 have strong affinity to H^+ in solution [42,43], can also accept electrons, thus act as active sites for H_2 generation, where the approaching electrons can directly react with the adsorbed H^+ from H_2O to produce H_2 [44,45]. Meanwhile, the sacrificial agent (TEOA) can be oxidized by the holes on CN-Py.

As reported by Grabowski and Rotkiewicz [46], nitrogen groups, which have lone pair electrons, often act as the electron donor, and aromatic rings act as electron acceptor, consequently, the charge carrier excitation and recombination process will take place in intramolecularly donor-acceptor conjugated copolymers. According to our previous work, the number of photoinduced electrons located at the acceptor in CN-Py is comparable to those at the LUMO level in g-C_3N_4 [9]. Compared with the photoexcited electrons from the intrinsic HOMO-LUMO transition in g-C_3N_4, the excited electron in the donor will transfer across the interface to the acceptor, and therefore will have much longer lifetime and less chance to recombine with holes, which is also beneficial to the efficient separation of charge carriers [9]. Furthermore, the CB of CN-Py is higher than that of g-C_3N_4 as demonstrated by Mott-Schottky analysis (Fig. 6), indicating the photogenerated electrons in CN-Py have stronger photoreduction ability than those in g-C_3N_4. This also contributes to the effective suppression of the S^{2-} and/or S_2^{2-} oxidation in MoS_2/CN-Py as demonstrated by XPS analysis, i.e., inhibiting the MoS_2 degradation and ensuring the high stability of the composite catalysts under visible light illumination.

5. Conclusions

In summary, a new kind of composite photocatalysts of MoS_2 nanoflower grown on pyridine-modified graphitic carbon nitride (CN-Py) have been successfully prepared *via* a solvothermal method. This kind of hetero-structure MoS_2/CN-Py endows the catalyst with significant visible light sensitivity, highly efficient separation and transfer of charge carriers, and consequently, greatly enhances photocatalytic performance in hydrogen production by water splitting under visible light irradiation. The optimum photocatalytic H_2 evolution rate on 3% MoS_2/CN-Py reaches 25 μmol h^{-1}. In addition to the mutual activation between MoS_2 and CN-Py under visible light irradiation owing to the promoted charge carrier separation, in the intramolecular donor-acceptor conjugated polymers obtained by pyridine modification (CN-Py), photogenerated electrons can be effectively separated from photogenerated holes, transfer to MoS_2 and significantly suppress the oxidation of S^{2-} and/or S_2^{2-} in MoS_2, which would prevent MoS_2 from photo-corrosion and endow this heterostructured photocatalyst with substantially improved durability. This work shows a promising cost-effective composite photocatalyst made of earth-abundant elements (C, N, Mo and S) for H_2 evolution without adding any noble-metal co-catalyst.

Acknowledgement

The authors gratefully acknowledge financial support from National Key Basic Research Program of China (2013CB933200), National 863 plans projects (2012AA062703), National Natural Science Foundation of China (21177137), Youth Innovation Promotion Association of CAS (2012200) and Shanghai Technical Platform for Testing and Characterization on Inorganic Materials (14DZ2292900).

Appendix A. Supplementary data

Supplementary data associated with this article can be found, in the online version, at http://dx.doi.org/10.1016/j.apcatb.2016.02.060.

Notes and references

[1] K. Joya, Y. Joya, K. Ocakoglu, R. Krol, Angew. Chem. Int. Ed. 52 (2013) 10426–10437.
[2] A. Kudo, Y. Miseki, Chem. Soc. Rev. 38 (2009) 253–278.
[3] A. Fujishima, K. Hoda, Nature 238 (1972) 474–475.
[4] S. Yang, Y. Gong, J. Zhang, L. Zhan, L. Ma, Z. Fang, R. Vajtai, X. Wang, P.M. Ajayan, Adv. Mater. 25 (2013) 2452–2456.
[5] K. Wang, Q. Li, B.S. Liu, B. Cheng, W. Ho, J.G. Yu, Appl. Catal. B: Environ. 176–177 (2015) 44–52.
[6] J. Ding, L. Wang, Q. Liu, Y. Chai, X. Liu, W.-L. Dai, Appl. Catal. B: Environ. 176–177 (2015) 91–98.
[7] J. Zhang, G. Zhang, X. Chen, S. Lin, L. Möhlmann, G. Dołęga, G. Lipner, M. Antonietti, S. Blechert, X. Wang, Angew. Chem. Int. Ed. 51 (2012) 3183–3187.
[8] Z. Chen, P. Sun, B. Fan, Q. Liu, Z. Zhang, X. Fang, Appl. Catal. B: Environ. 170–171 (2015) 10–16.
[9] X. Fan, L. Zhang, R. Cheng, M. Wang, M. Li, Y. Zhou, J. Shi, ACS Catal. 5 (2015) 5008–5015.
[10] X. Fan, L. Zhang, M. Wang, W. Huang, Y. Zhou, M. Li, R. Cheng, J. Shi, Appl. Catal. B: Environ. 182 (2016) 68–73.
[11] J. Wang, Z. Guan, J. Huang, Q. Li, J. Yang, J. Mater. Chem. A 2 (2014) 7960–7966.
[12] T. Jia, A. Kolpin, C. Ma, R. Chan, W. Kwok, S. Tsang, Chem. Commun. 50 (2014) 1185–1188.
[13] M. Liu, F. Li, Z. Sun, L. Ma, L. Xu, Y. Wang, Chem. Commun. 50 (2014) 11004–11007.
[14] Z. Wang, J. Hou, C. Yang, S. Jiao, H. Zhu, Chem. Commun. 50 (2014) 1731–1734.
[15] M. Li, L. Zhang, X. Fan, Y. Zhou, M. Wu, J. Shi, J. Mater. Chem. A 3 (2015) 5189–5196.
[16] L. Zhang, H. Wu, Y. Yan, X. Lou, Energy Environ. Sci. 7 (2014) 3303–3306.
[17] M. Nguyen, P. Tran, S. Pramana, R. Lee, S. Batabyal, N. Mathews, L. Wong, M. Graetzel, Nanoscale 5 (2013) 1479–1482.
[18] T. Jaramillo, K. Jorgensen, J. Bonde, J. Nielsen, S. Horchn, I. Chorkendorff, Science 317 (2007) 100–102.
[19] L. Ge, C. Han, X. Xiao, L. Guo, Int. J. Hydrogen Energy 38 (2013) 6960–6969.
[20] W. Peng, X. Li, Catal. Commun. 49 (2014) 63–67.
[21] Y. Hou, A. Laursen, J. Zhang, G. Zhang, Y. Zhu, X. Wang, S. Dahl, I. Chorkendorff, Angew. Chem. Int. Ed. 52 (2013) 3621–3625.
[22] Y. Li, H. Wang, L. Xie, Y. Liang, G. Hong, H. Dai, J. Am. Chem. Soc. 113 (2011) 7296–7299.
[23] S. Yan, Z. Li, Z. Zou, Langmuir 25 (2009) 10397–10401.
[24] M. Bojdys, J. Muller, M. Antonietti, A. Thomas, Chem. Eur. J. 14 (2008) 8177–8182.
[25] F. Wu, Y. Liu, G. Yu, D. Shen, Y. Wang, E. Kan, J. Phy. Chem. Lett. 3 (2012), 3330–3034.
[26] X. Zheng, J. Xu, K. Yan, H. Wang, Z. Wang, S. Yang, Chem. Mater. 26 (2014) 2344–2353.
[27] S. Habisreutinger, L. Schmidt-Mende, J. Stolarczyk, Angew. Chem. Int. Ed. 52 (2013) 7372–7408.
[28] S. Cao, J. Low, J. Yu, M. Jaroniec, Adv. Mater. 27 (2015) 2150–2176.
[29] F. Xiao, S. Huang, H. Tao, J. Miao, H. Yang, B. Liu, Nanoscale 6 (2014) 14950–14961.
[30] H. Li, S. Gan, H. Wang, D. Han, L. Niu, Adv. Mater. 27 (2015) 6906–6913.
[31] S. Menga, X. Ye, X. Ning, M. Xie, X. Fu, S. Chen, Appl. Catal. B Environ. 182 (2016) 356–368.
[32] V. Etacheri, M. Seery, S. Hinder, S. Pillai, Chem. Mater. 22 (2010) 3843–3853.
[33] Y. Liu, C. Xie, H. Li, H. Chen, T. Zou, D. Zeng, J. Hazard. Mater. 196 (2011) 52–58.
[34] Y. Li, H. Zhang, P. Liu, D. Wang, Y. Li, H. Zhao, Small 9 (2013) 3336–3344.
[35] V. Koroteev, L. Bulusheva, I. Asanov, E. Shlyakhova, D. Vyalikh, A. Okotrub, J. Phys. Chem. C 115 (2011) 21199–21204.
[36] X. Guo, G. Cao, F. Ding, X. Li, S. Zhen, Y. Xue, Y. Yan, T. Liu, K. Sun, J. Mater. Chem. A 3 (2015) 5041–5046.
[37] H. Vrubel, D. Merki, X. Hu, Energy Environ. Sci. 5 (2012) 6136–6144.
[38] J. Shi, Chem. Rev. 113 (2013) 2139–2181.
[39] H. Li, Y. Zhou, W. Tu, J. Ye, Z. Zou, Adv. Func. Mater. 25 (2015) 998–1013.
[40] J. Su, X. Zou, G. Li, X. Wei, C. Yan, Y. Wang, J. Zhao, L. Zhou, J. Chen, J. Phys. Chem. C 115 (2011) 8064–8071.
[41] Z. Lu, H. Zhang, W. Zhu, X. Yu, Y. Kuang, Z. Chang, X. Lei, X. Sun, Chem. Commun. 49 (2013) 7516–7518.
[42] H. Zhao, Y. Dong, P. Jiang, H. Miao, G. Wang, J. Zhang, J. Mater. Chem. A 3 (2015) 7375–7381.
[43] D. Lang, T. Shen, Q. Xiang, ChemCatChem 7 (2015) 943–951.
[44] Z. Wu, B. Fang, Z. Wang, C. Wang, Z. Liu, F. Liu, W. Wang, A. Alfantazi, D. Wang, D.P. Wilkinson, ACS Catal. 3 (2013), 2101–2017.
[45] K. Chang, Z. Mei, T. Wang, Q. Kang, S. Ouyang, J. Ye, ACS Nano 8 (2014) 7078–7087.
[46] Z. Grabowski, K. Rotkiewicz, Chem. Rev. 103 (2003) 3899–4031.